Effects of Centroid Position on Running Performance of Bridge Inspection Robot BIREM-IV

Hyunwoo Song[1], Ryota Hatanaka[2], and Yogo Takada[3]

[1,3](Mechanical and Physical Engineering graduate school, Osaka City University, Japan)
[2](Mechanical Engineering, Osaka City University, Japan)

Abstract: Since the period of high economic growth, the deterioration of social infrastructure, such as bridges and tunnels, has become increasingly serious. To prevent ageing, this infrastructure requires periodic inspection and repair; however, inspection is costly and time-consuming and, hence, there is a strong demand for practical bridge inspection robots to reduce the associated cost and time of inspections. The bridge inspection robot BIREM-IV, as developed in a previous study, uses magnetic rimless wheel and is capable of free movement in steel structures, exhibiting a high running performance. However, because autonomous driving is desired for the practical bridge inspection robot BIREM-IV, it is necessary to install inspection devices — such as sensors and cameras — for localization, as well as determine the allowable weight and appropriate mounting positions. In this study, we examined how driving performance changes with changing weight and center of gravity via simulations, using a mechanical model of BIREM-IV. The simulation was developed based on the parameters of BIREM-IV, confirming that the simulation matches the actual machine. In addition, it was possible to determine the unstable positions of the robot's center of gravity — which resulted in falling or being unable to drive — via the mechanical model by changing the position of the center of gravity and the weight of the BIREM-IV.
Key Word: Bridge inspection, Four-wheel driving robot, Magnetic wheel.

I. Introduction

Social infrastructures, such as bridges and tunnels, are vital to the population's daily lives. However, their functionality has decreased over time. Most of these structures were built during periods of economic growth but more than 50 years have passed since then; this is equivalent to the useful lifespan of most bridges. According to data released by the Ministry of Land, Infrastructure, Transport, and Tourism in 2016, approximately 20 % of brides are currently 50 years old and this will increase to 44 % by 2026 and 72 % by 2036; i.e., most bridges will be aged in 20 years. As bridges age, problems — such as cracks, leaks, and corrosion — occur and there is an increased risk of falling rocks or collapse. Therefore, national and local governments are conducting periodic inspections to extend the life of bridges. Periodic inspections are based on visual observation by inspectors, who use scaffolding or a special-purpose vehicle. However, as the number of aging bridges has increased, the shortage of inspectors has become a problem. Some inspection methods — such as utilizing a special crane — require traffic regulation, which may cause further problems (e.g., traffic congestion). Therefore, inspection via robots has attracted increasing attention owing to lower incurred costs and improved safety.

Recently, various robots have been developed for bridge inspections [1–17]. In particular, three types of robots for inspection of steel bridges — i.e. flying, suspension, and adsorption — are being studied. The flying-type robot can photograph the inspection surfaces of any structure, including concrete bridges, as long as there is space for the robot to enter [1–6]. However, this type of robot is easily affected by disturbances, such as wind or contact with the bridge. In addition, it exhibits problems such as a short operating time due to its significant power consumption, even when hovering.

The suspension-type robot moves across the lower surface of the bridge by installing anchors on the main body of the bridge or fishing the robot from the upper surface of the bridge [7–9]. Therefore, there is no risk of falling, more stable travel is possible (compared to flying- or magnet-type robots), and various inspections are possible, depending on the suspension method. However, there are various problems, e.g.,, it takes time to install the wires and bars necessary for moving and the safety of the robot and installation is difficult on a wide bridge.

The adsorption-type robot consumes almost no energy when the robot is stationary and can be inspected for a longer time than the flying type [10–16]. In addition, it is suitable for contact-type inspection

methods because it travels in contact with the structure. However, there are various problems, such as the need to travel complicated routes, moving to the inspection surface, and difficulties in eliminating the risk of falling.

Therefore, a four-wheeled robot bridge inspection robot equipped with Magnets version IV (BIREM-IV) was developed in a previous study, allowing movement in a three-dimensional and complex environment of steel bridges [16]. This robot uses magnetic rimless wheels and is capable of free movement in steel structures. However, because a practical bridge inspection robot is required to run autonomously, it is necessary to install inspection devices, such as sensors or cameras, for localization, as well as to determine the allowable weight and appropriate mounting position. In this study, we examine the driving performance of BIREM-IV as the weight and center of gravity change, using a mechanical model.

II. Permanent magnet bridge inspection robot BIREM-IV

Figure 1 shows an image of the BIREM-IV and its specifications are listed in Table 1. As shown in Figure 2, BIREM-IV is not only able to move on the ceiling and walls but can also move between horizontal and vertical planes, such as the floor-to-wall and wall-to-ceiling transitions of paths $1 - 8$.
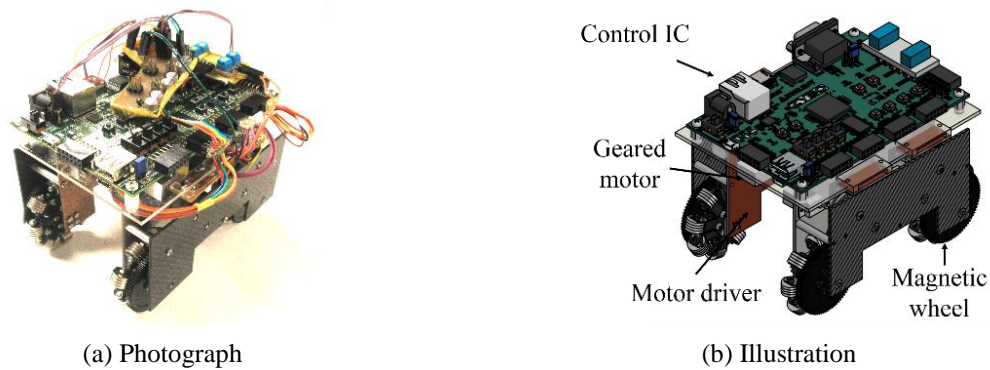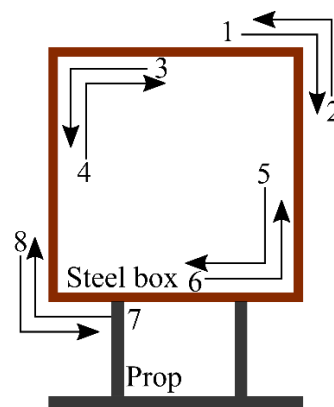

(a) Photograph   (b) Illustration

FIG. 1 BIREM-IV

Table no1: Specifications of BIREM-IV

Parameter	Value	Unit
Size	$140.0 \times 102.0 \times 123.0$	mm
Distance between left and right wheels	66.0	mm
Distance between front and rear wheel	90.0	mm
Mass of wheel	0.037	kg
Mass of chassis	0.339	kg
Wheel radius	24.0	mm
Control IC	Xilinx Zynq-7000 (XC7Z010-1CLG400C)	

(a) Photograph   (b) Illustration
FIG. 2 Various paths including a plane-to-plane transition such as floor-to-wall and wall-to-ceiling

As shown in Figure 3, the drive motor torque of BIREM-IV, the friction torque of the reduction mechanism, the attractive force acting between the magnet at the tip of the spoke and the wall surface, and the contact force are modeled, describing the behavior of the actual machine [16–18]. A previous study was conducted to identify the mechanical model so that it could be reproduced. BIREM-IV has three degrees of freedom $x_c = (x \quad y \quad z)^T$ for translational motion in the local coordinate system $\{c\}$, three degrees of freedom $\alpha = (\alpha \quad \beta \quad \gamma)^T$ for Euler angles that represent the posture of the unit, and four degrees of freedom that indicate the rotation angle of each wheel. Hence, we use a mechanical model with a total of 10 degrees of freedom, including $\widetilde{\theta} = (\theta_{FR} \quad \theta_{FL} \quad \theta_{RR} \quad \theta_{RL})^T$, and define these physical quantities as the fundamental variable $q = (x \quad y \quad z \quad \alpha \quad \beta \quad \gamma \quad \theta_{FR} \quad \theta_{FL} \quad \theta_{RR} \quad \theta_{RL})^T$.
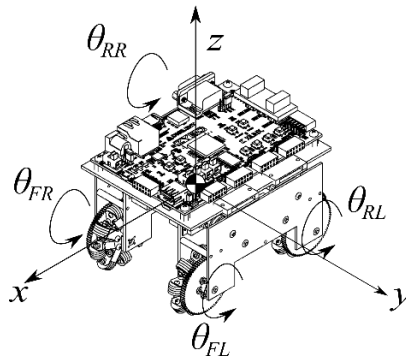

FIG. 3 Local coordinate system $\{c\}$

III. Simulation to measure the stable center of gravity position

In this experiment, the changes in running performance with changing weight and position of the center of gravity of the robot change were examined from simulations of the BIREM-IV mechanical model.

3.1 Simulation overview

This section provides an overview of the simulations. As shown in Figure. 4, the newly introduced local coordinate system $\{R\}$ has the same axis orientation as $\{c\}$ and the origin is the coordinate system at the center of gravity of the robot.
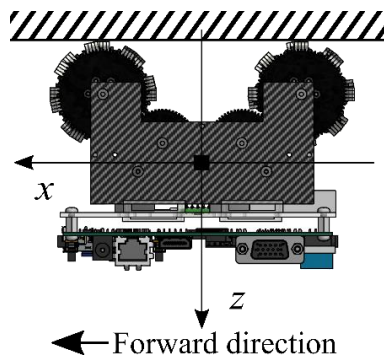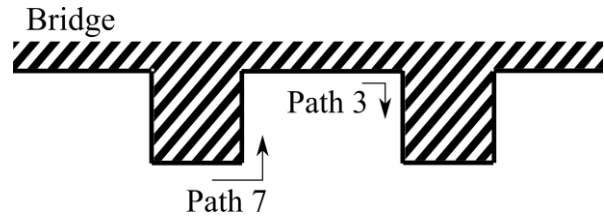

FIG. 4 Local coordinate system $\{R\}$

To measure the position of the stable center of gravity of the robot, the simulation is executed by adjusting the origin of the coordinate system $\{c\}$ while changing the center of gravity $x_{\text{shift}} = (x_{\text{shift}} \quad 0 \quad z_{\text{shift}})^T$ of BIREM-IV in 10 mm increments on the xz-plane of the local coordinate system $\{R\}$. Then, the boundary where BIREM-IV falls or travel becomes impossible is recorded and the area where it can run is investigated. Two patterns were performed: first, the weight of BIREM-IV was increased by 0.5 kg and, second, the weight was increased by 1.0 kg. In addition, BIREM-IV is intended to move on the lower part of the bridge, which is often obscured from sight, as shown in Figure 5. Therefore, in this experiment, we simulated four paths: running on the ceiling, climbing the wall, path 3, and path 7. The operating time of the simulation for

assessing performance was 5 s for running on the ceiling and flat running on the wall and 20 s for running at the corners of paths 3 and 7.

(a) Photograph   (b) Illustration

FIG. 5 Bridge inspection paths

3.2 Comparison between simulation and actual machine

Table 2 lists the basic parameters used in this study. These are based on data from an actual machine, obtained in a previous study. The simulation is executed via changing the position of the center of gravity by adjusting the origin of the coordinate system $\{c\}$ [16].

Table no2: Specifications of BIREM-IV

Parameters	Symbol	Value	Unit
Internal resistance of battery	R_b	0.145	Ω
Supply voltage	E_b	7.4	V
Acceleration of gravity	g_o	9.80665	m/s^2
Internal resistance of motor	R_M	4.8	Ω
Inductance of motor	L_M	140.0	μH
Inertia tensor of chassis	I_C^C	$\begin{pmatrix} 3.94 & -0.03 & 0.01 \\ -0.03 & 3.86 & 0.47 \\ 0.01 & 0.47 & 5.73 \end{pmatrix} \times 10^{-4}$	kg $\cdot$ m^2
Inertia tensor of rimless wheel	I_W^C	$\begin{pmatrix} 4.46 & 0 & 0 \\ 0 & 4.46 & 0 \\ 0 & 0 & 7.56 \end{pmatrix} \times 10^{-6}$	kg $\cdot$ m^2
Distance between gravity center of chassis and that of front wheel along x-axis of $\{c\}$ coordinate system	L_f	44.817	mm
Distance between gravity center of chassis and that of rear-wheel along x-axis of $\{c\}$ coordinate system	L_r	45.183	mm
Distance between gravity center of chassis and that of left wheel along y-axis of $\{c\}$ coordinate system	W_L	32.61	mm
Distance between gravity center of chassis and that of right wheel along y-axis of $\{c\}$ coordinate system	W_R	40.618	mm
Distance between gravity center of magnet along x-axis of $\{c\}$ coordinate system	W_m	1.624	mm
Distance between gravity center of chassis and that of rimless wheel along z-axis of $\{c\}$ coordinate system	H_w	46.168	mm
Thickness of rimless wheel	h_w	16.24	mm
Length of spoke	L_s	18.985	mm
Diameter of magnet	D_m	10.0	mm
Thickness of four magnets	H_m	6.0	mm
Mass of chassis	m_c	0.270	kg
Mass of rimless wheel	m_w	0.037	kg

The results of comparing the behavior of the actual machine with simulations using these and identified parameters are shown in Figures 6 and 7. From these results, it was confirmed that the behavior of the simulation and actual machine were almost the same.
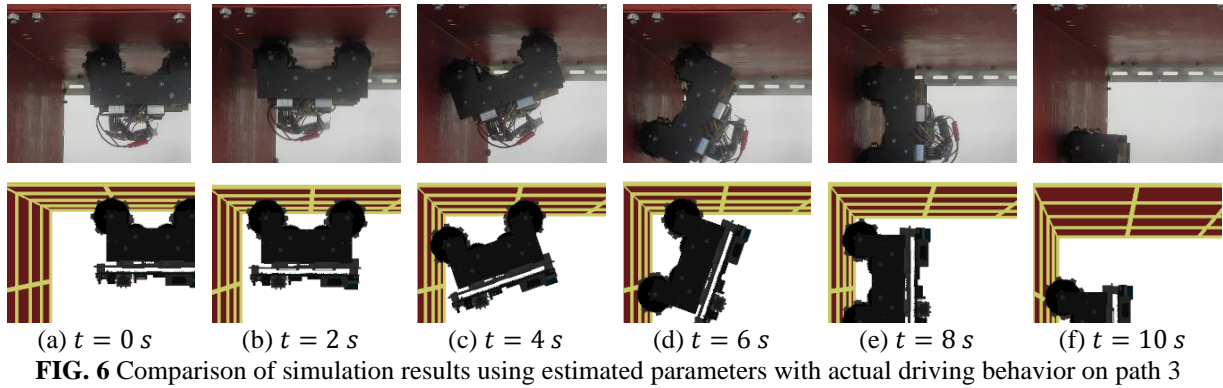
| (a) $t = 0\ s$ | (b) $t = 2\ s$ | (c) $t = 4\ s$ | (d) $t = 6\ s$ | (e) $t = 8\ s$ | (f) $t = 10\ s$ |

FIG. 6 Comparison of simulation results using estimated parameters with actual driving behavior on path 3

| (a) $t = 0\ s$ | (b) $t = 2\ s$ | (c) $t = 4\ s$ | (d) $t = 6\ s$ | (e) $t = 8\ s$ | (f) $t = 10\ s$ |
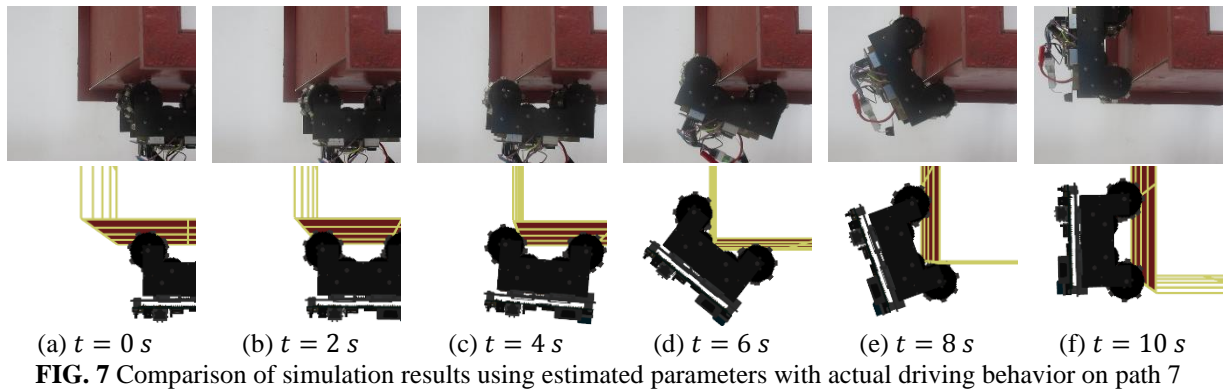
FIG. 7 Comparison of simulation results using estimated parameters with actual driving behavior on path 7

3.3 Simulation results
3.3.1 Results of ceiling and wall running

Figure 8 shows the stability discrimination results of simulating running on the ceiling and walls. For ceiling travel, it can be seen that the stability is likely to be affected when the center of gravity moves in the x-axis direction and that the effect is slight when the center of gravity moves in the z-axis direction. In the ceiling surface simulation, when most running is impossible, one wheel detached from the steel structure and the entire robot then fell while rotating. It is proposed that this is due to insufficient magnet adsorption power for canceling the moment that rotated the robot.

In the case of wall climbing, it can be seen that the stability is likely to be affected when the center of gravity moves in the z-axis direction and that the effect is slight when the center of gravity moves in the x-axis direction. In addition, as in the case of running on the ceiling surface, after one of the wheels detached from the steel structure, the robot fell while spinning. Therefore, it is thought that the reason for the inability to travel is that the attractive force of the magnet was insufficient to cancel the moment rotating the robot.
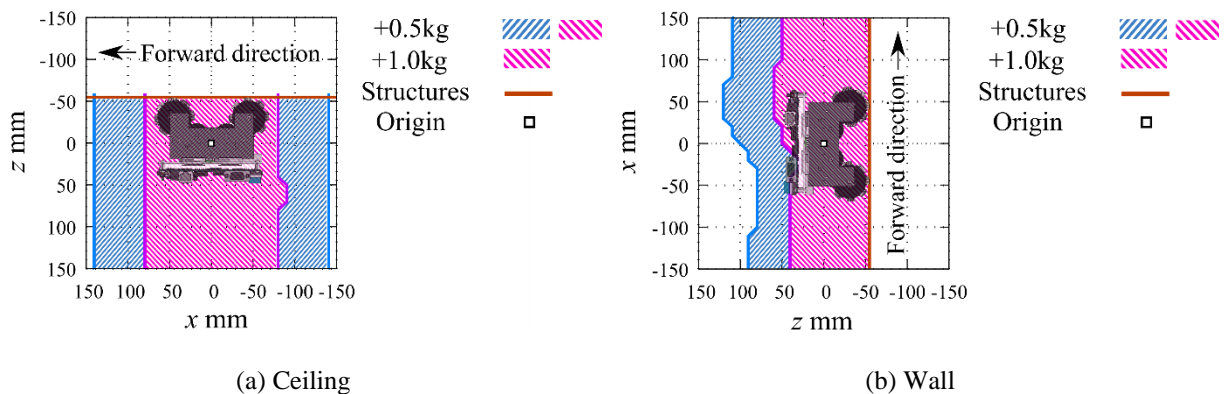

| (a) Ceiling | (b) Wall |

FIG. 8 Simulation results for ceiling and wall.

As shown in Figure 9, when traveling on the ceiling, it can be seen that the magnetic force required at the center of gravity is extremely close to or exceeds the maximum attractive force of 11.34 N. However, in the case of wall climbing, the wheel detached at less than the maximum attractive force. This is because upward

acceleration is required and so a force greater than that due to gravity is applied and the friction between the rear wheels and wall surface increases. Therefore, because the anti-torque of the rear wheel motor is applied in the same direction as the moment of force due to gravity, the force to peel off the front wheels may exceed the maximum magnetic force of the front wheel magnets.

From the above, it is considered that the robot cannot run on a flat surface because the attractive force of the wheel magnet is insufficient to cancel the moment that rotates the robot. In addition, when the robot climbs the wall surface, the force is greater than that due to gravity and it is necessary to consider the position of the center of gravity accordingly for running.
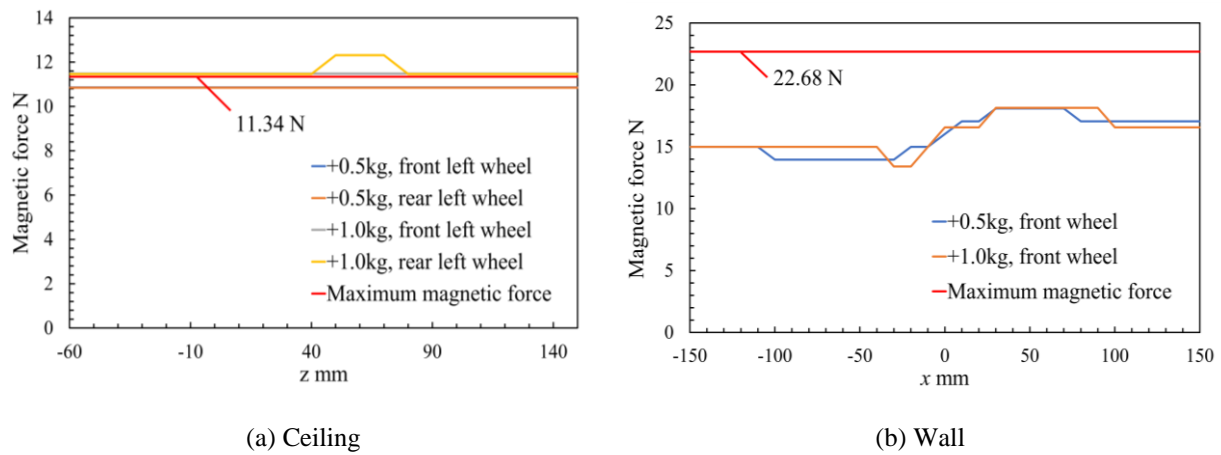

| (a) Ceiling | (b) Wall |

FIG. 9 Required magnetic force

3.3.2 Results of path 3 and path 7 running

Figure 10 shows the stability results of the robot simulating paths 3 and 7. For path 3, it becomes unstable when the center of gravity moves in the positive direction of the z-axis and the negative directions of the z-axis and x-axis, respectively, as shown in Figure 10(a). Conversely, in the case of path 7, it becomes unstable when the center of gravity moves in the positive direction of the z-axis and the positive direction of the x-axis, as shown in Figure 10(b).

In the area where travel on the ceiling surface is possible, it was often impossible to travel because of the slipping of the magnet while traveling on path 3. Therefore, it is considered that the path between the wall surfaces requires a greater force than usual at specific center of gravity positions.
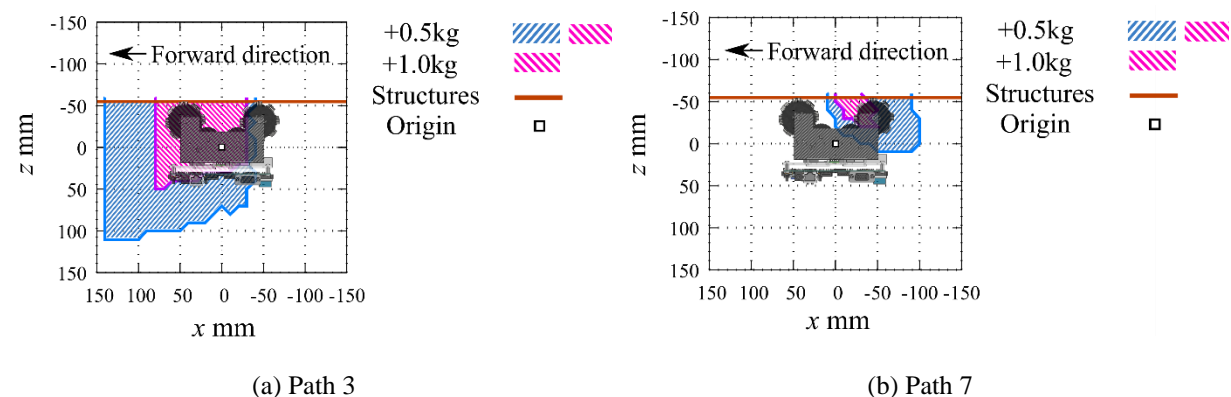

| (a) Path 3 | (b) Path 7 |

FIG. 10 Simulation results for path 3 and path 7.

The moment applied to the robot by gravity is considered for paths 3 and 7. From the results shown in Figure 10, the forces applied to the front and rear wheels at the center of gravity when travel becomes impossible are set to F_f and F_r, respectively. Therefore, in areas where the robot cannot run, the magnetic force and motor torque of the wheels (attempting to move the robot in the moving direction) are considered insufficient.
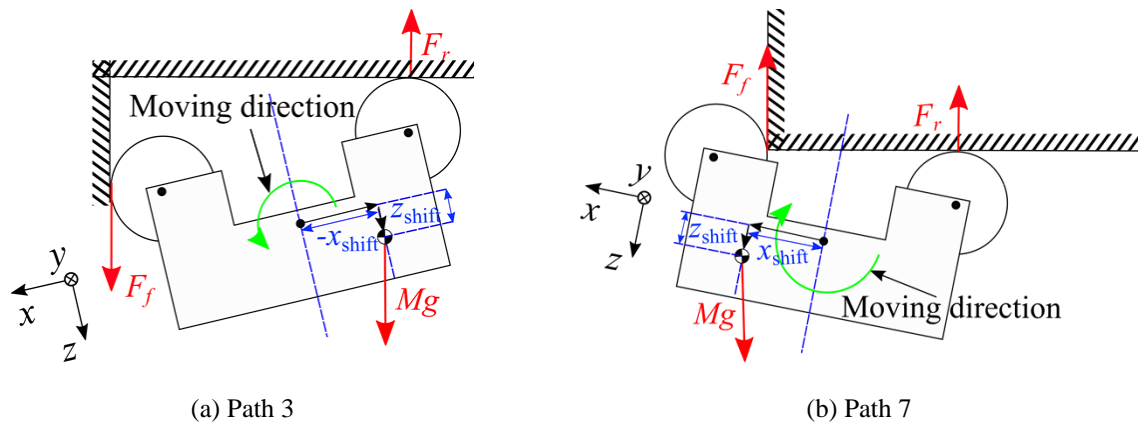
(a) Path 3　　　　　　　　　　　　　　　　(b) Path 7

FIG. 11 Turning power of BIREM-IV

3.3.3 Identification of stable center position using an interpolation method

Figure 12 shows the results of the four-path experiment. Based on the results, it can be seen that BIREM-IV has the highest stability when the center of gravity is slightly backward and low, relative to the direction of travel. However, even when the additional weight is 0.5 kg, it is difficult to design accordingly because the area in which driving is possible is narrow.
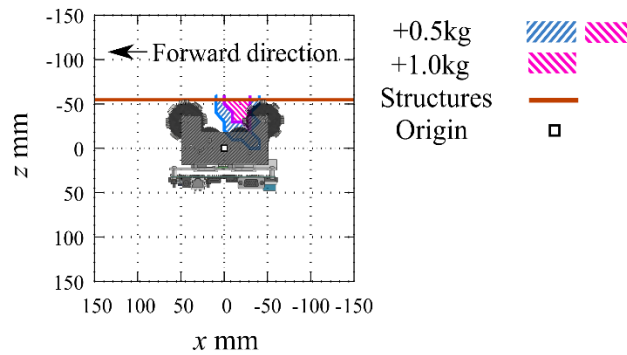

FIG. 12 Stability discrimination results obtained from the experimental results of 4 paths

Therefore, existing results and simulation results without additional weight are predicted using interpolation methods to ensure safety when the additional weight is less than 0.5 kg. Interpolation was calculated as the distance l_m from the geometric center of the region, with an additional weight of 1.0 kg to the boundary of the region, with an additional weight of m kg, using the following equation:

$$l_m = \frac{l_{0.5}}{2}\left\{\frac{1}{x_{0.5}}(a_1 m^2 + b_1 m + c_1) + \frac{1}{z_{0.5}}(a_2 m^2 + b_2 m + c_2)\right\} \tag{1}$$

where the reference point is the linear distance $l_{0.5}$, the directional distance $z_{0.5}$, and the directional distance $x_{0.5}$ to the boundary of the additional weight (0.5 kg).

However, a_1, b_1, c_1, a_2, b_2, and c_2 are constants that satisfy equations (2) and (3).

$$x_m = a_1 m^2 + b_1 m + c_1 \quad (m = 0.0, 0.5, 1.0) \tag{2}$$

$$z_m = a_2 m^2 + b_2 m + c_2 \quad (m = 0.0, 0.5, 1.0) \tag{3}$$

As shown in Figure 13, the distance to the x-axis in the positive direction from the geometric center of the region, with an additional weight of 1.0 kg to the boundary of the region with an additional weight of m kg is defined as x_m and the distance to the z-axis positive direction is defined as z_m.
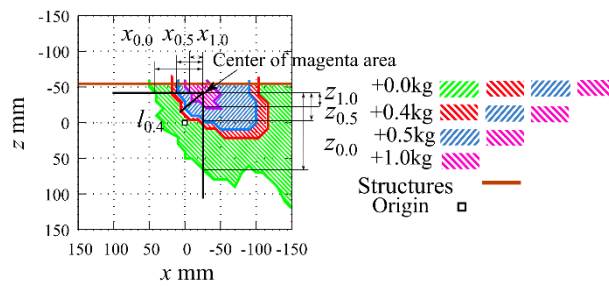
FIG. 13 Distance from center of magenta area to border lines

Figure 14(a) shows the stability discrimination result of path 7, including the interpolation result when the additional weight is 0.4 kg. Comparing this with the results of the actual simulation shown in Figure 14(b), they are roughly consistent. From Figure 14, it can be seen that the spatial range of the center of gravity that permits travel is expanded in both the x-axis and z-axis directions when there is no additional weight. The range was especially wide in the z-axis direction. Based on these results, it is thought that stable driving will be possible if the additional weight is reduced to approximately 0.4 kg and the center of gravity is mounted slightly backward.
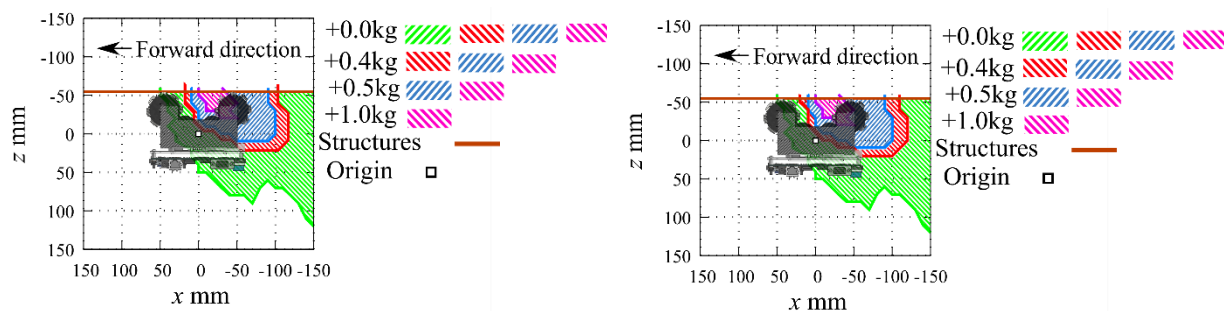
(a) Predictions on running possible area   (b) Running possible area
FIG. 14 Comparison between predictions and actual simulation result on additional weight 0.4 kg

IV. Conclusion

In this study, it was clarified that when the bridge inspection robot BIREM-IV was equipped with instrumentation devices and sensors necessary to realize bridge inspection through autonomous driving, a simulation study was conducted based on a mechanical model to determine the appropriate mounting position and allowable weight. Based on the mechanical model created by the previous study, we conducted simulations in which the position of the center of gravity and weight was changed to determine the runnable areas.

In this experiment, it was possible to grasp the unstable center of gravity position of the robot falling or unable to drive through the mechanical model that changed the center of gravity position and weight of the BIREM-IV. Based on this result, it is possible to facilitate redesign for mounting instrumentation devices and sensors, rather than repeating experiments on an actual machine. Next, by considering the moment applied to the static robot, we were able to consider the factors that make it impossible for the magnetic bridge inspection robot to travel on a plane surface. In addition, in the case of a moving path between the horizontal and vertical planes, the factors that increase the load for a specific central position can be considered. Finally, using the interpolation method based on the simulation results for loading weights of 0.0 kg, 0.5 kg, and 1.0 kg, it was possible to infer the range of the driving center position of the un-simulated loading weight. As a result, it is expected that stable running is possible if an additional weight of less than 0.4 kg is mounted so that it is located slightly behind the original center of gravity.

In the future, based on the results of this experiment, we will redesign the robot so that stable-running can be achieved on all paths, with the instrumentation device and sensors mounted on BIREM-IV. In addition, the results will be applied to the autonomous driving research of BIREM-IV using instrumentation devices and sensors.

References

[1].   Y. Okada, T. Okatani, Development of UAV with Passive Rotating Spherical Shell for Bridge Inspection and its Evaluation of Inspection Capability in Real Bridges, Journal of the Robotics Society of Japan, Vol. 34(2016), No. 2, pp. 119–122 (in Japanese).

[2].   N. Kanehira, M. Hirai, S. Kashimoto S. Echigo, Bridge Mounting Multicopter for Bridge Inspection, Kawada Technical Report, Vol. 36(2017), pp. 22–28 (in Japanese).

[3].   Y. Takada, Y. Tokura, Y. Matsumura, T. Tanaka, T. Kanada, Wall Inspection Robot with Maneuvering Assist Control System Against Crosswind, Journal of Robotics and Mechatronics, Vol. 30(2018), No. 3, pp. 416–425.

[4].   M. Nakao, E. Hasegawa, T. Kudo, N. Sawasaki, Development of a Bridge Inspection Support Robot System Using Two-Wheeled Multicopters, Journal of Robotics and Mechatronics, Vol. 31(2019), No. 6, pp. 837–844.

[5].   K. Hidaka, D. Fujimoto, K. Sato, Autonomous Adaptive Flight Control of a UAV for Practical Bridge Inspection Using Multiple-Camera Image Coupling Method, Journal of Robotics and Mechatronics, Vol. 31(2019), No. 6, pp. 845–854.

[6].   P. Chun, J. Dang, S. Hamasaki, R. Yajima, T. Kameda, H. Wada, T. Yamane, S. Izumi, K. Nagatani, Utilization of Unmanned Aerial Vehicle, Artificial Intelligence, and Remote Measurement Technology for Bridge Inspections, Journal of Robotics and Mechatronics, Vol. 32(2020), No. 6, pp. 1245–1258.

[7].   R. Fujisawa, K. Umemoto, M. Tanaka, N. Sato, N. Nagaya, M. Katsuyama, Development, Bridge Inspection and Operation of Araneus - Winch Wiring Robot System, J. JSCE. Ser. F4, (Construction and management) Special Issue, Vol. 73(2017), No. 1, pp. 26–37 (In Japanese).

[8].   K. Nakata, K. Umemoto, K. Kaneko, F. Ryusuke, Development and Operation of Wire Movement Type Bridge Inspection Robot System ARANEUS, Kalpa Publications in Engineering, Vol. 3(2020), pp. 168–174.

[9].   H. Kajiwara, N. Hanajima, K. Kurashige, Y. Fujihira, Development of Hanger-Rope Inspection Robot for Suspension Bridges, Journal of Robotics and Mechatronics, Vol. 31(2019), No. 6, pp. 855–862.

[10].   Mazumdar, A. and Asada, H.H., Mag-Foot: A steel bridge inspection robot, Intelligent Robots and Systems, IROS 2009 IEEE/RSJ International Conference on 2009(2009), pp. 1691–1696.

[11].   Y. Takada, S. Ito, N. Imajo, Development of a bridge inspection robot capable of traveling on splicing parts, Inventions, Vol. 2(2017), No. 3, pp. 22.

[12].   W. Lee, S. Hirose, Contacting Surface-Transfer Control for Reconfigurable Wall-Climbing Robot Gunryu III, Journal of Robotics and Mechatronics, Vol. 25(2013), No. 3, pp. 439–448.

[13].   R. Wang, Y. Kawamura, An Automated Sensing System for Steel Bridge Inspection Using GMR Sensor Array and Magnetic Wheels of Climbing Robot, Journal of Sensors, Vol. 2016(2016), Article ID 8121678.

[14].   Y. Matsumura, T. Shiba, S. Ito, Y. Kawase, Y. Takada, Development of Magnetic Bridge Inspection Robot Aimed at Carrying Heavy Loads, International Journal of Robotic Engineering, Vol. 3(2018), No. 2.

[15].   H. M. La, T. H. Dinh, N. H. Pham, Q. P. Ha, A. Q. Pham, Automated Robotic Monitoring and Inspection of Steel Structures and Bridges, Robotica, (2016), pp. 1–21.

[16].   Y. Matsumura, K. Kawamoto, Y. Takada, Development of a Compact Wall-Climbing Robot Capable of Transitioning among Floor, Vertical Wall and Ceiling, Journal of the Robotics Society of Japan, Vol. 37(2019), No. 6, pp. 514–522 (in Japanese).

[17].   Y. Takada, Y. Matsumura, K. Nakajima, Development of Nonlinear Dynamic Model of Wall-Climbing Robot BIREM-IV and Application of State Feedback Control, The Proceedings of the Dynamics & Design Conference, Vol. 2019 (2019), pp. 434 (in Japanese).

[18].   Y. Ohkami, Coordinate Transformation Algorithm by the Eulerian Angles Representation, Space Technology Research Group, National Aerospace Laboratory (NAL), TR-305(1972), pp. 1–13 (In Japanese).